JGR Space Physics

METHOD
10.1029/2021JA030249

Key Points:

- REPTile-2 is a miniaturized particle telescope measuring electrons and protons with fine energy resolution and minimal contamination
- This study highlights the key role of anticoincidence detectors in reducing contamination and improving measurement quality
- Detailed Geant4 simulations have proved to be instrumental in characterizing instrument response and potential contamination sources

Supporting Information:

Supporting Information may be found in the online version of this article.

Correspondence to:

L.-Y. Khoo,
leng.khoo@colorado.edu

Citation:

Khoo, L.-Y., Li, X., Selesnick, R. S., Schiller, Q., Zhang, K., Zhao, H., et al. (2022). On the challenges of measuring energetic particles in the inner belt: A Geant4 simulation of an energetic particle detector instrument, REPTile-2. *Journal of Geophysical Research: Space Physics*, *127*, e2021JA030249. https://doi.org/10.1029/2021JA030249

Received 27 DEC 2021
Accepted 23 MAR 2022

On the Challenges of Measuring Energetic Particles in the Inner Belt: A Geant4 Simulation of an Energetic Particle Detector Instrument, REPTile-2

L.-Y. Khoo[1,2], X. Li[1,2], R. S. Selesnick[3], Q. Schiller[4], K. Zhang[1,2,4], H. Zhao[5], B. Hogan[1,2], J. T. Cantilina[2], A. Sims[2], E. Bauch[1,2], T. Valade[2], S. Boyajian[2], and R. Kohnert[2]

[1]Department of Aerospace Engineering Sciences, University of Colorado Boulder, Boulder, CO, USA, [2]Laboratory for Atmospheric and Space Physics, University of Colorado Boulder, Boulder, CO, USA, [3]Space Vehicles Directorate, Air Force Research Laboratory, Kirtland AFB, Albuquerque, NM, USA, [4]Now at Space Science Institute, Boulder, CO, USA, [5]Physics Department, Auburn University, Auburn, AL, USA

Abstract Following the retirement of the community supported Van Allen Probes mission, the quest for high-quality energetic particle measurements in the radiation belts is likely to be taken on by smaller spacecraft like CubeSats in the foreseeable future. Here we introduce the Relativistic Electron Proton Telescope integrated little experiment-2 (REPTile-2), a miniaturized (~1.5 U) solid-state charged particle telescope that aims to undertake this challenging task. It incorporates detailed pulse-height analysis to enable 60 electron channels and 60 proton channels and includes anticoincidence detectors to minimize unwanted background contamination. This paper presents a description of the REPTile-2 design and emphasizes the importance of extensive Geant4-based analysis to inform the design of a new energetic particle detector and characterize the instrument response. Our analysis shows that REPTile-2 can measure ~0.3–~4 MeV electrons and ~6.7–35 MeV protons with energy resolution (ΔE/E) of 7%–38% for electrons and 1.5%–5% for protons. Results from a Sr-90/Y-90 radioactive source test have verified the instrument performance and the validity of the Geant4 simulations. These energetic particle measurements will enable a new scientific understanding of the inner radiation belt, where unwanted contamination from the unforgiving penetration of highly energetic protons (tens of MeV to GeV) is common, and provide detailed quantification of the inner belt electrons and protons in the low-Earth orbit that is crucial for space weather modeling.

1. Introduction

High-quality measurements of energetic particles can shed light on old, lingering questions and provide a new perspective on our prior understanding of the radiation belts. For instance, one of the perplexing findings from the Van Allen Probes mission is the absence of MeV electrons in the inner belt (Fennel et al., 2015; Li et al., 2015, Li, Baker, et al., 2017). This observation contrasts with previous findings such as those of Baker et al. (2004), Zheng et al. (2006), and Li et al. (2009), where significant > MeV fluxes from previous missions were observed in the inner belt during the early 2000s. Inspired by Van Allen Probes measurements, Selesnick (2015b) reexamined observations from the early 2000s and suggested that equatorial trapping electron measurements in the inner belt were overwhelmed by lower energy electrons or high-energy protons, leaving the task of characterizing these stably trapped MeV electrons for the future. On the other hand, the theoretical prediction of the CRAND contribution to high-energy inner radiation belt electrons (>800 keV) has not been verified by observation due to a lack of high-sensitivity detectors (Selesnick, 2015a), while the CRAND contribution to quasi-trapped ~0.5 MeV electrons has been clearly identified (for example, Li, Selesnick, et al., 2017). To address these questions requires fine-energy resolution and low contamination energetic particle measurements.

Measuring energetic particles, especially electrons, can be a daunting task, as explained by Vampola (1998). It requires an understanding of how particles of interest and background populations interact with the instrument. In addition to background contamination, for example, from highly energetic protons and bremsstrahlung radiation by highly energetic electrons, electronic limitations such as saturation add additional complexity to identifying the energies and species of incident particles correctly. In an ideal system, the electronics can handle and resolve every single pulse triggered by incident particles. In reality, the electronics cannot distinguish pulses that occur within the resolution time (pileup) and require some time to recover after recording a pulse (deadtime). A coincidence system might also be tricked by two different particles that hit almost simultaneously on two different

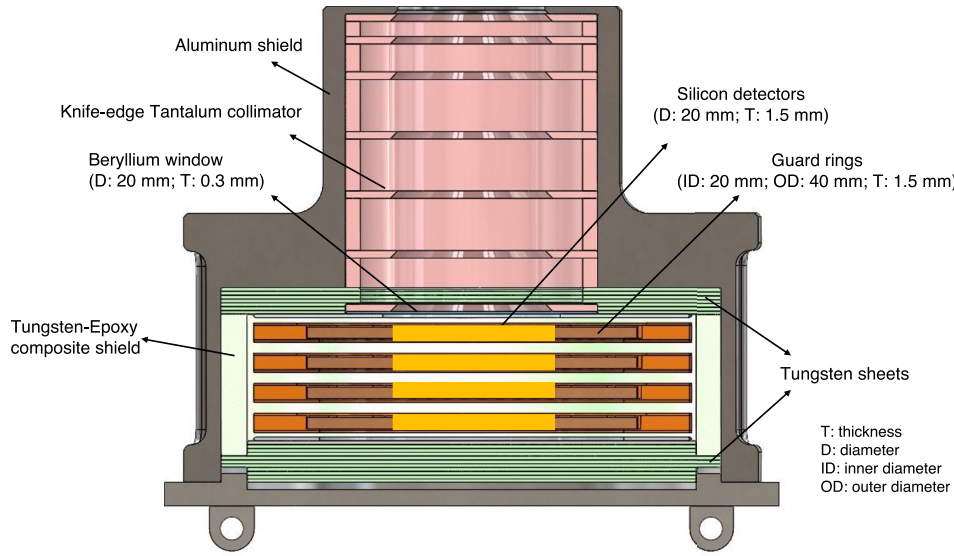

Figure 1. Illustration of REPTile-2 design with key features labeled.

detectors and interpret them as a single particle (chance coincidence). Previous instruments have suffered from these detrimental effects in the inner belt region, where actual measurements are sometimes overwhelmed (Selesnick, 2015a; Selesnick et al., 2019). To ensure the quality of energetic particle measurements, it is thus necessary to consider and understand the effect of these potential problems early in the instrument design phase.

The Relativistic Electron Proton Telescope integrated little experiment-2 (REPTile-2) is a miniaturized solid-state telescope that has been designed with these specific challenges in mind. The goal is to provide fine energy resolution measurements with minimal background contamination or electronic limitations. REPTile-2 has flight heritage from REPT (Baker et al., 2012) onboard Van Allen Probes and REPTile onboard the Colorado Student Space Weather Experiment (CSSWE) CubeSat (Blum & Schiller, 2012; Li et al., 2012, Li, Palo, et al., 2013, Li, Schiller, et al., 2013; Schiller & Mahendrakumar, 2010). With the addition of guard rings and pulse-height analysis, REPTile-2 has improved upon the previous design; through Geant4 simulations and calibration results, it demonstrates capability for providing 300 keV–3 MeV electron measurements with energy resolution as low as 40 keV ($\Delta E/E < 17\%$ for 300–500 keV) and in minimizing unwanted background contamination. REPTile-2 is the sole payload onboard the Colorado Inner Radiation Belt Experiment (CIRBE), a low-Earth orbit (LEO) CubeSat mission supported by NASA. It is designed to constantly point at directions perpendicular to the local magnetic field lines. The mission is currently scheduled for launch no earlier than the fourth quarter of 2022.

The purpose of this paper is to provide a description of REPTile-2 design and a detailed discussion of instrument performance that is characterized with the aid of Geant4 simulations. This paper concludes with a Sr-90/Y-90 test result that verifies the validity of Geant4 simulations and the functionality of the instrument.

2. REPTile-2 Design

REPTile-2 is a ~1.5 U (10 × 10 × 15 cm, with electronics) energetic particle telescope, as illustrated in Figure 1. It includes four 1.5 mm thick silicon detectors separated into inner areas (a diameter of 20 mm) and outer rings (inner diameter: 20 mm; outer diameter: 40 mm), which are also known as guard rings. The silicon detectors are obtained from Micron Semiconductors, UK. Each silicon detector is held in the center of a detector holder with a separation of 2.5 mm between two detectors.

In front of the silicon detectors, there is a beryllium (Be) window with a diameter of 20 mm and a thickness of 0.3 mm that can block <~200 keV electrons and <~6 MeV proton from reaching the silicon detectors. In front of the Be window, a collimator, with a total length of ~40.5 mm and seven optimally spaced, knife-edge baffles, is used to prevent electrons outside the field of view (FOV) from entering the detector stack directly (Schiller &

Mahendrakumar, 2010). The collimator has an inner radius of 10 mm and is mainly made of Tantalum (Ta), a high atomic number (Z) material. Under this configuration, REPTile-2 has a ∼51° FOV.

The entire instrument is shielded by aluminum (Al) with an additional inner shield made of mostly Tungsten (W) that surrounds the silicon detectors. The thickness of the Al shield on REPTile-2 ranges between 0.1 and 10 mm, while the thickness of the W shield ranges from 3.5 mm on the side to 5 mm on the back. This layered shield stops electrons with energies less than ∼10 MeV and protons with energies less than ∼60 MeV from reaching the detector stack. Tungsten sheets, ∼0.5 mm thick each, are used on the top and bottom of the detector stack, while the inner Tungsten shield ring around the detector stack is made of Tungsten-epoxy composite (64% Tungsten and 36% epoxy). These changes are made to meet the orbital debris requirement during atmospheric reentry for spacecraft de-orbit. The overall mechanical design is inherited from REPTile with some changes such as the use of guard rings for all four detectors and a thinner Be window to decrease the lower energy limit of measurable particles.

3. Geant4 Simulations

Geant4 (abbreviation for Geometry And Tracking, version 4) is an object-oriented toolkit that uses a Monte-Carlo approach to simulate the passage of particles through matter (Agostinelli et al., 2003; Allison et al., 2006, 2016). In this study, all simulations were performed using Geant4.10.6. source code. The standard Geant4 electromagnetic physics list G4EmStandardPhysics_option4 ("EMZ") is selected for this study. This study conducted two types of simulations: a boresight-shooting simulation and a "spherical simulation" where particles of a randomized incident energy shoot from an inner spherical surface around the instrument. The former informs us about the instrument responses to field-of-view (FOV) particles, while the latter allows us to explore the detector's responses to particles from and outside the FOV. We utilized the G4General Particle Source package available in Geant4 for the spherical simulations. The radius of the source sphere is 50 mm, centered at the beryllium window to cover the entire instrument. The angular distribution of the incident particles is prescribed a cosine-law distribution to generate an isotropic flux inside the sphere. Incident electrons and protons that range from 0.1 to 10 MeV and 1–200 MeV, respectively, are simulated in a randomized order. Tens of billions of events were simulated to ensure sufficient statistics. The energies deposited on all four detectors and guard rings for each event were recorded and analyzed using MATLAB 2017b software.

4. Instrument Characterization

4.1. Anticoincidence Detectors – The Guard Rings

Very energetic protons can penetrate the passive shielding and be a source of contamination for electron measurements. To mitigate this, REPTile-2 uses anticoincidence detectors for active collimation. As a critical feature of the REPTile-2 design, these guard rings are employed to detect and remove all particles that deposit higher than a specified threshold, TG. Figure 2a illustrates all simulated energy deposits by incident protons on the third detector, D3, and the last detector, D4. Figure 2b shows only events where the guard rings are not triggered. The contrast between Figures 2a and 2b (without and with guard-ring triggers) is apparent. A vast amount of side-penetrating, high-energy protons are removed by using the guard rings in anticoincidence.

The bottom panel of Figure 2 presents a similar comparison but for incident electrons. Unlike Figures 2a and 2b, fewer "contaminated" events are removed in Figure 2f, and the energy deposits by incident electrons also have no distinct pattern. The simulated incident electrons (0.1–10 MeV) deposit lower energies (<5 MeV) than incident protons. This is not surprising because the stopping power for electrons is smaller, and thus electrons deposit/lose less energy than protons when traversing the same thickness material. It is also worth noting that the simulated results in Figure 2 are from the spherical Geant4 simulations based on a flat incident energy spectrum, while in reality, the incident particles more closely follow an exponential or power-law energy spectrum. As a result of this realistic particle distribution, the number of very energetic incident particles that are removed by the anticoincidence logic will be much smaller in the actual space environment. For instance, ∼92.5% (∼24%) of protons (electrons) were removed by the guard rings using the flat energy spectrum, and the removal percentage reduces to ∼14% for protons and ∼2% for electrons using a more realistic energy spectrum from AP9 and AE9.

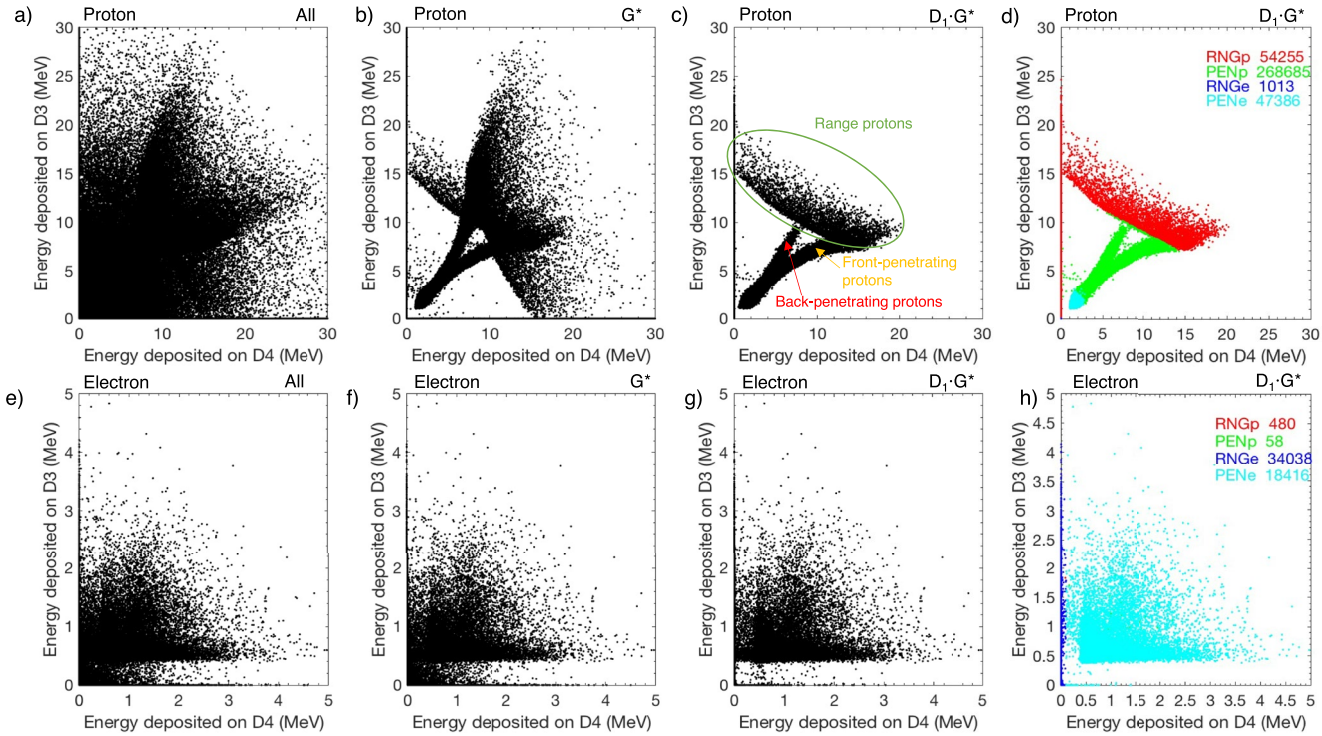

Figure 2. Energy deposition on the third detector (D3) against the energy deposition on the fourth detector (D4). The top and bottom panels are those by incident protons and electrons, respectively. (a & e) All events without applying the anticoincidence logic. (b & f) Only events that do not trigger the guard rings (i.e., energy deposit ≤ TG). (c & g) Events that do not trigger the guard ring and deposit energy > TD on the first detector, which are required to be considered as valid events in this study. (d & h) shows how the valid events are categorized into different particle types (red for RNGp, green for PENp, blue for RNGe, and cyan for PENe). TD and TG are the threshold of the minimum energy deposit on a detector and guard rings (0.1 and 0.671 MeV in this case), respectively. A flat incident flux spectrum is used here for both protons and electrons. The simulated electron and proton energy ranges are 0.1–10 MeV and 1–200 MeV, respectively.

4.2. Logic and Binning Equations

In this study, a valid event is an event that does not trigger the guard rings (i.e., energy deposit on guard rings is less than or equal to TG) and deposit energies above a certain threshold, TD, on the first detector. TD and TG are set as 100 and 671 keV based on the electronic noise analysis where the standard deviation of the electronic noise on each detector is ∼15–20 keV. Examples of the valid events from incident protons and electrons, which deposited energies on D_3 and D_4, are presented in Figures 2c and 2g, respectively. With the addition of D_1 requirements, the resultant valid event plot further reduces the contamination from mostly back-penetrating particles, demonstrated in comparisons between Figures 2b and 2c and between Figures 2f and 2g. Above all, it reveals "footprints" of distinct incident proton populations: range (RNG) protons (which deposit all their energy in the detector stack) and penetrating (PEN) protons (which deposit little energy in the detector stack). These "footprints" prove to be helpful in deriving the logic equations for characterizing incident particles. The valid events are then categorized into four different particle types: range proton (RNGp), penetrating proton (PENp), range electron (RNGe), and penetrating electron (PENe). Table 1 summarizes the logic equations, which are explained in detail below. Thresholds like TD, TG, and the values in slant equations, D_{12s} and D_{34s}, can be modified during flight.

Table 1
Logic Equations for Each Particle Type Used in REPTile-2

Particle types	Logic equations
Range proton (RNGp)	$D_1 \cdot D_{12s} \cdot (D_4^* + D_{34s}) \cdot G^*$
Penetrating proton (PENp)	$D_1 \cdot D_{12s} \cdot D_4 \cdot D_{34s}^* \cdot G^*$
Range electron (RNGe)	$D_1 \cdot D_{12s}^* \cdot D_4^* \cdot G^*$
Penetrating electron (PENe)	$D_1 \cdot D_{12s}^* \cdot D_4 \cdot G^*$

Note. · is logical AND; + is logical OR; * is logical complement (NOT). E_n = measured energy deposit in detector n. $G_t = G_1 + G_2 + G_3 + G_4$. D_n is true if E_n > TD. G is true if G_t > TG. D_{12s} is true if $E_1/2.8$ MeV + $E_2/4.2$ MeV > 1. D_{34s} is true if $E_3/13.5$ MeV + $E_4/30$ MeV > 1.

To distinguish electrons from protons, we recalled that the energy deposits by incident electrons are significantly lower than those by incident protons. This distinction allows the derivation of an empirical slant equation, D_{12s}. Particles that fulfill D_{12s} requirement deposit relatively high energy on the first two detectors and hence are most likely incident protons. The valid proton events are further binned into RNGp and PENp using another slant equation D_{34s} and D_4 requirement (i.e., energy deposited on the last detector must be

greater than TD). Energetic protons (>30 MeV) that enter from the FOV can penetrate through the detector stack and deposit very little energy in the detector stack. This is shown in Figure 2c, where the valid events have two distinct branches and a negative-slope population. The fork is made of very energetic penetrating protons (>30 MeV): one branch is formed by front-penetrating protons, which deposit more energy on D_4 than D_3; the other is formed by back-penetrating protons, which deposit more energy on D_3 than D_4. On top of the fork, there is a notable population with a negative slope, which is a characteristic of range protons. They distinctively deposit much higher energies in the last two detectors than the penetrating protons. Utilizing this characteristic difference, we derived another slant equation, D_{34s}, that is useful to distinguish the range proton that stops on the last detector from the penetrating protons, while the D_4 requirement captures the range protons that stop on the first three detectors. Together, they help differentiate range protons from penetrating protons (See Figure S1 in Supporting Information S1 for more details).

Due to electron scattering and range straggling, which cause the lack of defined characteristics in the electron's energy deposit distribution (Figure 2f), it is not possible to differentiate range electrons from penetrating electrons, unlike for incident protons (Bichsel, 1988; Li et al., 2015). Instead, a more simplistic approach is taken: PENe is defined as a valid event that deposits > TD energy on the last detector (namely, the D_4 criteria in Table 1), while those that do not fulfill the D_4 requirement are considered as RNGe. Figures 2d and 2h illustrate how valid events are categorized into different particle types using the logic equations. Most events are correctly categorized into their corresponding species channels. However, there are a small number of high-energy protons that deposit very little energy and are incorrectly identified as electrons (cyan dots in Figure 2d). Compared to protons, most events by incident electrons are correctly identified by logic equations as electrons, and only a very small portion of incident electrons that deposit sufficient energies on D_1 and/or D_2 and fulfill D_{12s} requirements are incorrectly identified as protons.

The valid events for each particle type are then binned into different energy channels based on their total energy deposit in all four detectors. Due to the electronic noise, only energy deposits higher than the threshold, TD, on each detector are included in the computation of the total energy deposit. There is a total of 129 channels for REPTile-2. The first 120 channels are all logarithmically spaced differential channels except the last channel for each particle classification, which is an integral channel (i.e., Ch 50 for RNGp, Ch 60 for PENp, Ch 110 for RNGe, and Ch 120 for PENe. Also see Tables S1, S2, and S3 in Supporting Information S1). RNGp and RNGe channels have 50 channels each, and PENp and PENe channels have ten channels each. The last nine channels include four channels that record counts of events that have >TD energy deposit on each detector (D_1, D_2, D_3, and D_4) and another four that record the coincidence range data ($D_1 \bullet D_2$*, $D_1 \bullet D_2 \bullet D_3$*, $D_1 \bullet D_2 \bullet D_3 \bullet D_4$*, and $D_1 \bullet D_2 \bullet D_3 \bullet D_4$). The last channel, 129, records the count of events on the guard rings (G). A detailed breakdown of the required total energy deposition for RNGp, RNGe, PENe, and PENp channels is recorded in Tables S1, S2, and S3 in Supporting Information S1.

4.3. Energy Response Functions

Response functions are commonly used to describe how efficiently an instrument detects particles with a given incident energy, species, and angle. The energy response function, using Geant4 simulation results, is obtained by $Gr_i(E) = \frac{n_i(E)}{N(E)} 4\pi^2 r^2$, where n_i is the number of valid events for channel i, N is the total simulated events, E is the incident energy, i refers to channel i, and r is the radius of the source sphere in Geant4. This is equivalent to multiplying the geometry factor of the sphere, $4\pi^2 r^2$, by the fraction of incident particles that trigger channel i, n_i/N. Spherical simulation results based on a uniform incident flux spectrum are used in the computation. The resultant response function is independent of the choice of the source sphere size (so long as it encloses the entire detector) because an increase in the radius of the source sphere will decrease the number of valid events for each channel and, in turn, yield the same response function. The full response functions for the RNGp and RNGe channels can be found in Figures 3a and 3b, and the response functions for PENp and PENe channels are shown in Figure S2 in Supporting Information S1. The incident energy steps in these figures are 100 and 10 keV for protons and electrons, respectively.

It is notable in Figures 3a and 3b that each channel is generally well-resolved, suggesting that the logic and binning equations are sufficient at categorizing the particles and the simulation statistics are adequate. These figures include the contributions of particles from inside and outside the FOV. For example, the hump around

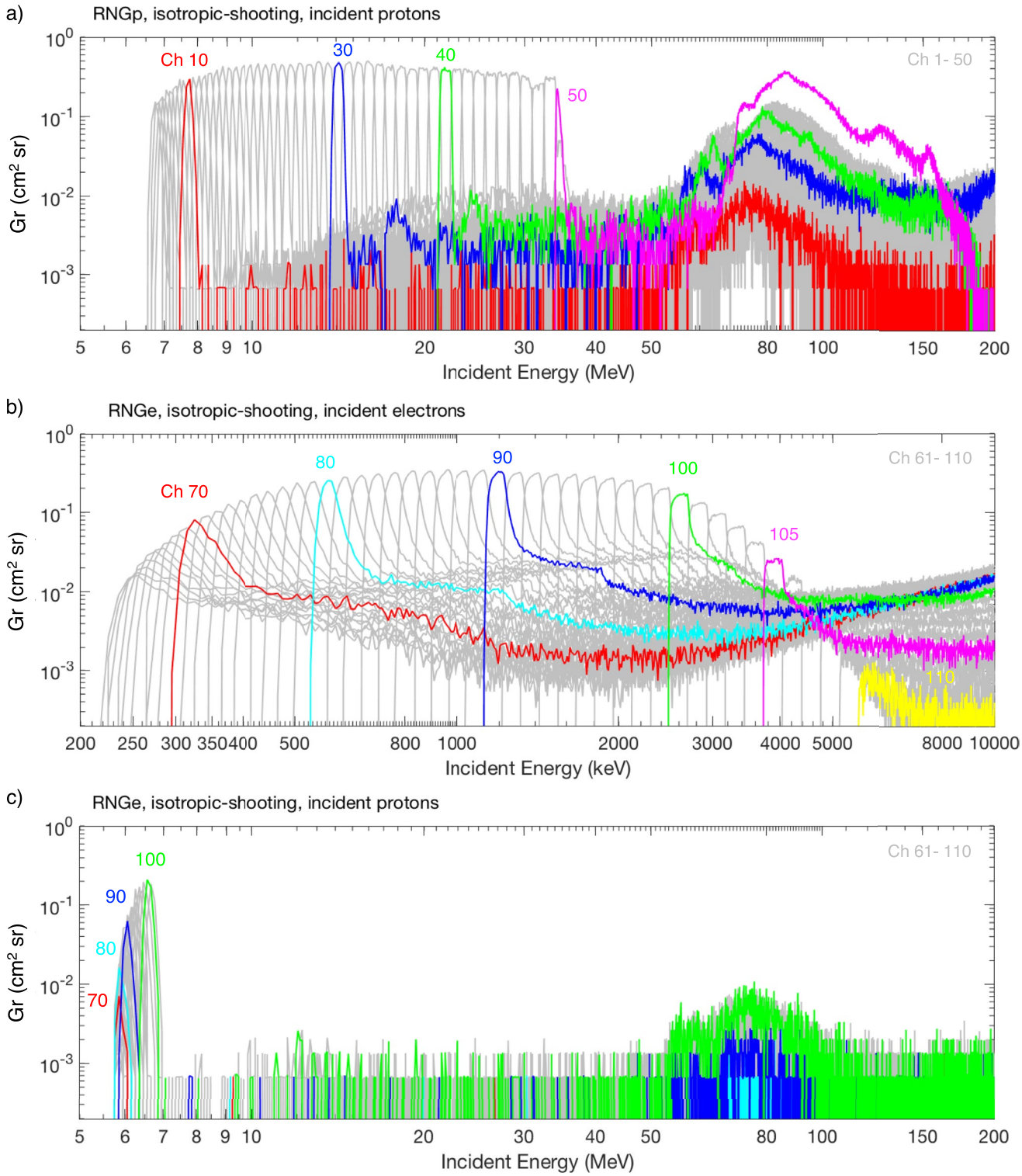

Figure 3. (a) & (b) Energy response functions for incident protons and electrons. Different colors represent response functions for channels: (a) RNGp channels, Channels 1–50; (b) RNGe, Channels 61–110. The highlighted channels are Channels 10 (red), 30 (blue), 40 (green), and 50 (magenta) for RNGp; Channels 70 (red), 80 (cyan), 90 (blue), 100 (green), 105 (magenta) and 110 (yellow) for RNGe. A flat incident flux spectrum is used here for both protons and electrons. The simulated electron and proton energy ranges are 0.1–10 MeV and 1–200 MeV, respectively. (c) Energy response functions of incident protons for RNGe channels (Channels 61–110): channel 70 (red), 80 (cyan), 90 (blue), and 100 (green).

60–100 MeV protons (Figure 3a) indicates that these protons are energetic enough to penetrate through the Al-W layered shielding at a specific angle that does not trigger guard rings and deposit a small amount of energy on the detectors, appearing as lower energy protons. This population will be monitored using PENp channels and corrected whenever necessary.

A nominal energy resolution is determined by the full width at half maximum of the response function for each channel. Quantitively, the nominal energy resolution ($\Delta E/E$) is between 7% and 38% for RNGe channels and 1.5% and 5% for RNGp channels, which is a vast improvement from its predecessor, REPTile (with resolution between 80% and 95% for electron channels and 29% and 67% for proton channels). A nominal energy response is an average of the corresponding energy response within the nominal energy width for each channel. The nominal energy for RNGp and RNGe channels corresponds to $E < 35$ MeV for proton and $E < \sim 6$ MeV for electrons, and their nominal energy response ranges from 0.001 to 0.28 cm^2sr for RNGe channels and 0.1–0.4 cm^2sr for RNGp channels. The nominal energy response and energy resolutions for each channel in RNGp and RNGe are summarized in Tables S1 and S2 in Supporting Information S1.

To characterize the role of very energetic protons as background contamination to electron measurements, we have computed the response function of incident protons that get binned into electron channels (Figure 3c). Low energy (~6–7 MeV) protons that barely make it through the Be window have a comparable geometric factor (0.02–0.2 cm^2sr for Channel 80–100), and this could be a significant background concern for electron measurements (~0.6–~3 MeV). These energetic protons generally exist in the inner belt only, except during solar proton events when they have access to higher L (>3.5) (for example, Filwett et al., 2020). Since energetic electron fluxes are much greater at higher L (>3.5), the effect of proton contamination on electron measurements at higher L is generally less severe. In other words, the potential contamination from these low-energy protons will likely occur when the spacecraft goes through the center of the inner belt and will be tracked accordingly.

4.4. Pileup Effect

We also examine the pileup effect on REPTile-2. The minimum time resolution between two events, τ, is 400 ns, that is, a pileup-free count is recorded if no additional events occur within 400 ns. Before determining the pileup rate, the count rate is computed using the energy response function on the respective detector and the AE9/AP9 flux spectrum. The count rate, $r(E)$, is approximated as $r(E) = Gr(E)j(E)\Delta E$, where E is the incident energy, ΔE is the incident energy bin width (1 MeV for protons and 0.1 MeV for electrons), $Gr(E)$ is the energy response function, and $j(E)$ is the estimated flux according to the trapped energetic electron and proton model (AE9 and AP9 model) (Ginet et al., 2013). The mean electron and proton flux spectra as a function of geographical longitude and latitude are obtained from AE9 and AP9 models, assuming that the satellite orbits at an inclination of 97-degree and an altitude of 600 km (the highest allowable altitude limit for a CubeSat with no active de-orbit mechanism like CIRBE, in accordance with the FCC guidelines (https://docs.fcc.gov/public/attachments/DOC-358437A1.pdf). To model the "worst-case" scenario, we selected an energy spectrum inside the South Atlantic Anomaly (SAA) region where fluxes of most energies are high for the pileup analysis.

Since Geant4 simulates an ideal detector that can resolve every pulse (or event), the computed count rate from Geant-4 simulations is a pileup-free count rate, as indicated by red lines in Figure 4. The two-event pileup rate is computed based on the assumption that the superposition only involves two pulses that occur within the instrument resolution time (Knoll, 2000; Selesnick & Stone, 1991). The pileup count rate can be approximated as a summation between pileup-free events and events that were piled up to a specific channel with subtraction of events that would be in that specific channel but were piled up to a higher-energy channel. The results are shown as blue lines in Figure 4. The pileup analysis is conducted for the first detector, as it is subjected to the highest flux among all detectors. Figure 4 demonstrates that with a 0.3 mm thick Be window, the pileup count rates on detector 1 for lower-energy particles do not deviate much from the pileup-free count rate. When the pileup occurs, multiple lower energy pulses can appear as a single high-energy pulse. Consequently, the system (incorrectly) records smaller counts for lower energy particles and higher counts for higher energy particles. Figure 4 suggests that the pileup effect is negligible for protons but could be a problem for electrons in this worst-case scenario analysis. This will likely happen when the spacecraft goes through the SAA region, during which the pileup effect will be monitored and corrected when needed. In most observations outside of the SAA region, we expect the pileup effect to be relatively small and negligible.

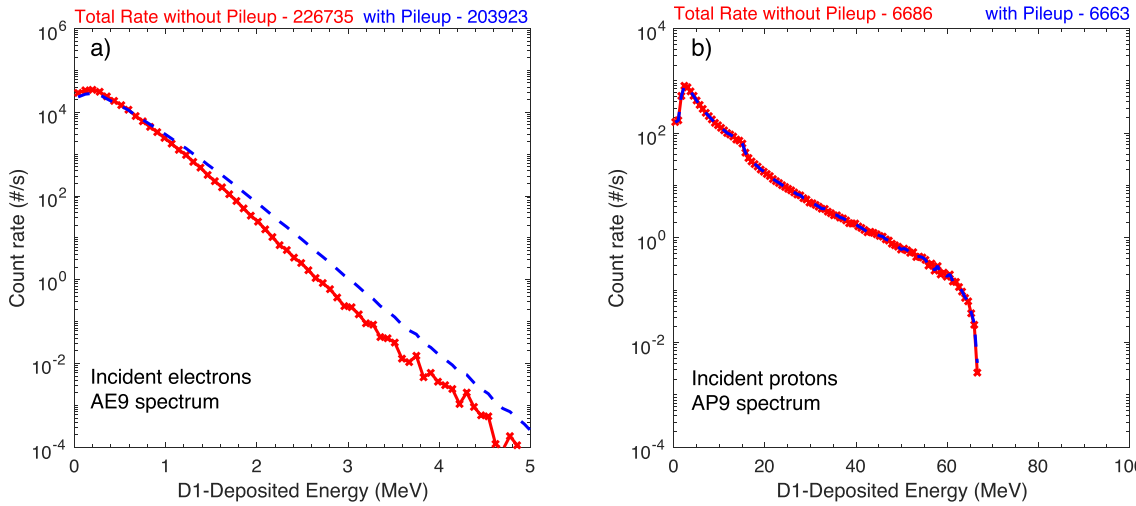

Figure 4. Count rate with and without two-event pileup on detector 1 for incident electrons (left) and protons (right).

5. Instrument Sr-90 Radioactive Source Test

We have performed a Sr-90/Y-90 radioactive source test on the flight REPTile-2 instrument to verify the instrument performance. The source was placed directly in front of the REPTile-2 aperture. Sr-90 has a half-life of 28.8 years and undergoes beta decay into Y-90, resulting in a maximum electron energy of 546 keV. With a half-life of 64 hr, Y-90 decays into the stable Zr-90 and produces a maximum energy of 2.3 MeV (NuDat, 2008).

The Sr-90 source used in this test is a <0.5 mm thin strontium plated onto a steel disk and was acquired in the late 2000s. Since the range of a 300 keV electron in Sr happens to be 0.5 mm, the thickness of the Sr source will have little influence on the energy range that we are interested to compare with. In addition, even as the source decays over time, its spectrum is likely unaffected since Sr-90 has a relatively long half-life (~29 years). Also note that this test was conducted in the laboratory and thus some of the lower energy electrons from the Sr-90 spectrum will be lost to the air when traversing through the collimator before reaching the Be window. Based on our Geant4 simulations and the ESTAR table (Berger et al., 2005), >200 keV electrons lose <8% of their initial energy in the air before arriving at the Be window. Since most of the <~200 keV electrons are blocked by the Be window, the loss of lower energy electrons in air will have little effect on our Sr-90 test result.

The black asterisks in Figure 5a show the measured count rates for these events. The relationship between count rate and flux is:

$$r_i = \int Gr_i(E) j(E) dE \quad (1)$$

where r_i is the count rate at channel i, $Gr_i(E)$ is the channel energy response, and $j(E)$ is flux spectrum as a function of energy, E. We used two different approaches to convert the count rate to flux: a bowtie method (Claudepierre et al., 2021; Selesnick & Blake, 2000) and a generalized least square method (Selesnick et al., 2018; Tarantola & Valette, 1982). The bowtie method is often used in space missions due to its simplicity of implementation, but it has some intrinsic disadvantages. For instance, its resolution is limited by the channel width. On the other hand, the generalized least square method is commonly used in geophysics to tackle the inverse problem and can yield a better-resolved flux spectrum, given a fine energy response function.

Figure 5b presents the estimated fluxes from both bowtie and generalized least squares method and their comparisons with the expected spectrum (Euramet, 2019). We converted estimated fluxes back to count rates using Equation (1) and compared estimated count rates to observed count rates to verify that the least squares solution is reasonable (Figure 5a). Figure 5b shows that estimated fluxes from both methods are in good agreement with the expected spectrum, which validates the instrument performance and Geant4 simulations. The uncertainty in the bowtie solution is estimated by propagating the statistical errors in the count rates to the final flux estimates. Overall, the uncertainty in the bowtie solution is small, except at $E > 2.1$ MeV. Compared to the solutions from

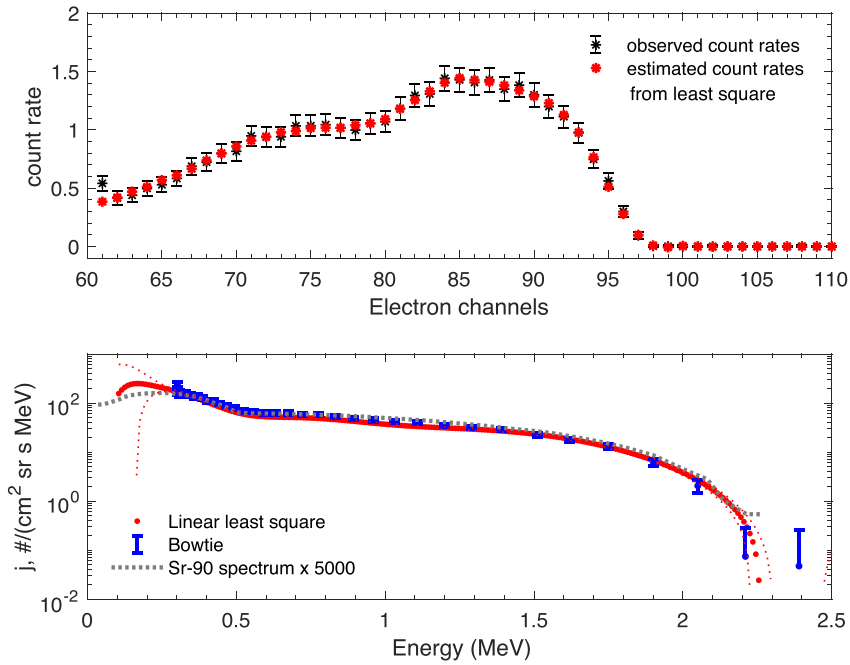

Figure 5. (a) Observed (black) and estimated (red) count rate from the least squares method for the Sr-90 source test. (b) Estimated flux from the bowtie method (blue) and least squares method (red), in comparison with the expected Sr-90/Y-90 spectrum (dotted gray curve). The dotted red curves and blue error bars show the uncertainties of the estimated flux from the least squares method and the bowtie analysis, respectively.

the bowtie method, the least squares solution yields a better-resolved energy spectrum. It provides an uncertainty estimate as indicated by the red dotted curve in Figure 5b. Higher uncertainty is associated with estimated fluxes for <300 keV electrons, as expected. It is also noted that since the lowest RNGe channel (Channel 61) measures only >220 keV electrons and has an FWHM energy range between 240 and 300 keV (based on its response function described in Figure 3b and Table S2 in Supporting Information S1), flux for <220 keV electrons using the least squares method is extrapolated and thus has a higher uncertainty. The solution uncertainty also increases near the end of the Sr-90/Y-90 spectrum at $E > 2.1$ MeV. We also noted that count rates are not exactly zero at higher energy (nominal energy, $\bar{E} > 2.3$ MeV) channels, namely electron channel 98 and above, possibly due to background radiation like muons. This explains why the bowtie analysis provides a very low flux (rather than zero) with a relatively large uncertainty at E ~ 2.4 MeV.

6. Final Remarks

This paper summarizes the comprehensive analysis involved in the design of the miniaturized solid-state charged particle instrument, REPTile-2. We would like to emphasize the critical role of Geant4 simulations in informing and improving the REPTile-2 design. Most of the analysis is aided by Geant4 simulations, including the derivation of the logic and binning equations, instrument characterization, and the study of the pileup effect on REPTile-2. A radioactive source test validated the Geant4 simulations and the performance of REPTile-2, providing fine energy resolution measurements for relativistic electrons. With the incorporation of pulse-height analysis and anticoincidence detectors, REPTile-2 has vastly improved performance relative to its predecessor instrument (REPTile), particularly in background reduction and energy resolution. The compact design of REPTile-2 also makes it suitable for small satellite missions.

Data Availability Statement

Simulated data used in this study is generated using the Geant4 source code that can be obtained from https://geant4.web.cern.ch and is publicly available at https://figshare.com/projects/REPTile-2_Geant4_simulation_data/134291.

Acknowledgments
The authors would like to thank the CIRBE team, present and past, for their invaluable contribution to this project. The authors also express gratitude to Guillem Megias i Homar, Mark Looper, Yang Mei, Declan O'Brien, Zheng Xiang, and Wenxun Zhang for their time and advice for improving this study. This work is not possible without the funding support from NASA grants 80NSSC18K1276, 80NSSC18K1119, and 80NSSC19K0237. This work utilized resources from the University of Colorado Boulder Research Computing Group, which is supported by the National Science Foundation (awards ACI-1532235 and ACI-1532236), the University of Colorado Boulder, and Colorado State University.

References

Agostinelli, S., Allison, J., Amako, k., Apostolakis, J., Araujo, H., Arce, p., et al. (2003). Geant4—A simulation toolkit. *Nuclear Instruments & Methods in Physics Research, Section A*, *506*(3), 250–303. https://doi.org/10.1016/S0168-9002(03)01368-8

Allison, J., Amako, K., Apostolakis, J., Arce, P., Asai, M., Aso, T., et al. (2016). Recent developments in Geant4. *Nuclear Instruments and Methods in Physics Research Section A: Accelerators, Spectrometers, Detectors and Associated Equipment*, *835*, 186–225.

Allison, J., Amako, K., Apostolakis, J. E. A., Araujo, H. A. A. H., Dubois, P. A., Asai, M. A. A. M., et al. (2006). Geant4 developments and applications. *IEEE Transactions on Nuclear Science*, *53*(1), 270–278. https://doi.org/10.1109/tns.2006.869826

Baker, D. N., Kanekal, S. G., Hoxie, V. C., Batiste, S., Bolton, M., Li, X., et al. (2012). The Relativistic Electron-Proton Telescope (REPT) instrument on board the Radiation Belt Storm Probes (RBSP) spacecraft: Characterization of Earth's radiation belt high-energy particle populations. *Space Science Reviews*, *179*, 337–381. https://doi.org/10.1007/s11214-012-9950-9

Baker, D. N., Kanekal, S. G., Li, X., Monk, S. P., Goldstein, J., & Burch, J. L. (2004). An extreme distortion of the Van Allen belt arising from the "Hallowe"en' solar storm in 2003. *Nature*, *432*, 878–881. https://doi.org/10.1038/nature03116

Berger, M. J., Coursey, J. S., Zucker, M. A., & Chang, J. (2005). *ESTAR, PSTAR, and ASTAR: Computer programs for calculating stopping-power and range tables for electrons, protons, and helium ions*. National Institute of Standards and Technology. [Online] Available:[2022, February 19] Retrieved from http://physics.nist.gov/Star

Bichsel, H. (1988). Straggling in thin silicon detectors. *Reviews of Modern Physics*, *60*(3), 663–699. https://doi.org/10.1103/revmodphys.60.663

Blum, L., & Schiller, Q. (2012). Characterization and testing of an energetic particle telescope for a CubeSat platform. In *Proceedings of the 26th annual AIAA/USU conference on small satellites*. SSC12-VIII-4. Retrieved from https://lasp.colorado.edu/home/csswe/files/2012/06/Blum-and-Schiller.pdf

Claudepierre, S. G., Blake, J. B., Boyd, A. J., Clemmons, J. H., Fennell, J. F., Gabrielse, C., et al. (2021). The magnetic electron ion spectrometer: A review of on-orbit sensor performance, data, operations, and science. *Space Science Reviews*, *217*, 80. https://doi.org/10.1007/s11214-021-00855-2

European Association of National Metrology (Euramet). (2019). *Radionuclide beta spectra metrology*. Retrieved from http://metrobeta-empir.eu/wp-content/uploads/2019/11/15SIB10_MetroBeta_Final_Publishable_Report.pdf

Fennell, J. F., Claudepierre, S. G., Blake, J. B., O'Brien, T. P., Clemmons, J. H., Baker, D. N., et al. (2015). Van Allen Probes show that the inner radiation zone contains no MeV electrons: ECT/MagEIS data. *Geophysical Research Letters*, *42*, 1283–1289. https://doi.org/10.1002/2014GL062874

Filwett, R. J., Jaynes, A. N., Baker, D. N., Kanekal, S. G., Kress, B., & Blake, J. B. (2020). Solar energetic proton access to the near-equatorial inner magnetosphere. *Journal of Geophysical Research: Space Physics*, *125(6)*, e2019JA027584. https://doi.org/10.1029/2019JA027584

Ginet, G. P., O'Brien, T. P., Huston, S. L., Johnston, W. R., Guild, T. B., Friedel, R., et al. (2013). AE9, AP9 and SPM: New models for specifying the trapped energetic particle and space plasma environment. *Space Science Reviews*, *179*, 579–615. https://doi.org/10.1007/s11214-013-9964-y

Knoll, G. (2000). *Radiation detection and measurement* (3rd ed.). John Wiley and Sons (ISBN: 9780471073383).

Li, X., Baker, D. N., Zhao, H., Zhang, K., Jaynes, A. N., Schiller, Q., et al. (2017). Radiation belt electron dynamics at low L (<4): Van Allen Probes era versus previous two solar cycles. *Journal of Geophysical Research: Space Physics*, *122*, 5224–5234. https://doi.org/10.1002/2017ja023924

Li, X., Barker, A. B., Baker, D. N., Tu, W. C., Sarris, T. E., Selesnick, R. S., et al. (2009). Modeling the deep penetration of outer belt electrons during the "Halloween" magnetic storm in 2003. *Space Weather*, *7*, S02004. https://doi.org/10.1029/2008SW000418

Li, X., Palo, S., Kohnert, R., Blum, L., Gerhardt, D., Schiller, Q., & Califf, S. (2013). Small mission accomplished by students—impact on space weather research. *Space Weather*, *11*, 55–56. https://doi.org/10.1002/swe.20025

Li, X., Palo, S., Kohnert, R., Gerhardt, D., Blum, L., Schiller, Q., et al. (2012). Colorado student space weather experiment: Differential flux measurements of energetic particles in a highly inclined low Earth orbit, in dynamics of the Earth's radiation belts and inner magnetosphere. In D. Summers (Ed.), (Vol. *199*, pp. 385–404). AGU.*Geophysical Monograph Series*.

Li, X., Schiller, Q., Blum, L., Califf, S., Zhao, H., Tu, W., et al. (2013). First results from CSSWE CubeSat: Characteristics of relativistic electrons in the near-Earth environment during the October 2012 magnetic storms. *Journal of Geophysical Research: Space Physics*, *118*(10), 6489–6499. https://doi.org/10.1002/2013JA019342

Li, X., Selesnick, R., Schiller, Q., Zhang, K., Zhao, H., Baker, D. N., & Temerin, M. A. (2017). Measurement of electrons from albedo neutron decay and neutron density in near-Earth space. *Nature*, *552*(7685), 382–385. https://doi.org/10.1038/nature24642-385

Li, X., Selesnick, R. S., Baker, D. N., Jaynes, A. N., Kanekal, S. G., Schiller, Q., et al. (2015). Upper limit on the inner radiation belt MeV electron intensity. *Journal of Geophysical Research: Space Physics*, *120*, 1215–1228. https://doi.org/10.1002/2014JA020777

National Nuclear Data Center, Brookhaven National Laboratory. (2008). NuDat (nuclear structure and decay data). Retrieved from https://www.nndc.bnl.gov/nudat2/

Schiller, Q., & Mahendrakumar, A. (2010). REPTile: A miniaturized detector for a CubeSat mission to measure relativistic particles in near-Earth space. In *Proceedings of the 24th annual AIAA/USU conference on small satellites*. SSC10-VIII-1. https://digitalcommons.usu.edu/smallsat/2010/all2010/43/

Selesnick, R. S. (2015a). High-energy radiation belt electrons from CRAND. *Journal of Geophysical Research: Space Physics*, *120*(4), 2912–2917. https://doi.org/10.1002/2014JA020963

Selesnick, R. S. (2015b). Measurement of inner radiation belt electrons with kinetic energy above 1 MeV. *Journal of Geophysical Research: Space Physics*, *120*, 8339–8349. https://doi.org/10.1002/2015JA021387

Selesnick, R. S., Baker, D. N., Kanekal, S. G., Hoxie, V. C., & Li, X. (2018). Modeling the proton radiation belt with Van Allen Probes relativistic electron-proton telescope data. *Journal of Geophysical Research: Space Physics*, *123*, 685–697. https://doi.org/10.1002/2017JA024661

Selesnick, R. S., & Blake, J. B. (2000). On the source location of radiation belt relativistic electrons. *Journal of Geophysical Research*, *105*(A2), 2607–2624. https://doi.org/10.1029/1999JA900445

Selesnick, R. S., & Stone, E. C. (1991). Energetic electrons at Uranus: Bimodal diffusion in a satellite limited radiation belt. *Journal of Geophysical Research*, *96*(A4), 5651–5665. https://doi.org/10.1029/90JA02696

Selesnick, R. S., Su, Y.-J., & Sauvaud, J.-A. (2019). Energetic electrons below the inner radiation belt. *Journal of Geophysical Research: Space Physics*, *124*, 5421–5440. https://doi.org/10.1029/2019JA026718

Tarantola, A., & Valette, B. (1982). Generalized nonlinear inverse problems solved using the least squares criterion. *Reviews of Geophysics*, *20*(2), 219–232. https://doi.org/10.1029/RG020i002p00219

Vampola, A. L. (1998). Measuring energetic electrons: What works and what doesn't? In R. F. Pfaff, J. E. Borovsky, & D. T. Young (Eds.), *Measurement techniques in space plasmas: Particles* (pp. 339–355). AGU. https://doi.org/10.1029/GM102p0339

Zheng, Y., Lui, A. T. Y., Li, X., & Fok, M.-C. (2006). Characteristics of 2–6 MeV electrons in the slot region and inner radiation belt. *Journal of Geophysical Research*, *111*, A10204. https://doi.org/10.1029/2006JA011748